Absence of ferromagnetism in ferroelectric Mn-doped BatiO3 nanofibers

María C. Maldonado-Orozco[a,b], Martha T. Ochoa-Lara[a], Jesús E. Sosa-Márquez[a], Roberto P. Talamantes-Soto[a], Abel Hurtado-Macías[a], Ricardo López Antón[c], Juan A. González[c], José T. Holguín-Momaca[a], Sion F. Olive-Méndez[a], Francisco Espinosa-Magaña[a*]

[a]*Centro de Investigación en Materiales Avanzados, S.C., Laboratorio Nacional de Nanotecnología. Miguel de Cervantes 120, Complejo Industrial Chihuahua, 31109 Chihuahua, Chihuahua, México*
[b]*Facultad de Ingeniería de la Universidad Autónoma de Chihuahua, México 31100*
[c]*Instituto Regional de Investigación Científica Aplicada (IRICA) and Departamento de Física Aplicada, Universidad de Castilla-La Mancha, 13071 Ciudad Real, Spain.*

Abstract

Pure and Mn-doped barium titanate nanofibers were synthesized by the electrospinning method. The morphology, microstructure and crystal structure of as-spun and annealed composite nanofibers were characterized by scanning electron microscopy and transmission electron microscopy. After annealing at 850 °C, we obtain nanofibers a few μm long, formed by nanoparticles of irregular shape with sizes around 100 nm. X-ray diffraction and Raman spectroscopy show that a partial phase transition from tetragonal to hexagonal takes place for $BaTi_{0.90}Mn_{0.10}O_3$. Vibrational phonon modes were calculated for $BaTiO_3$ within the density functional theory (DFT) framework. Ferroelectricity has been probed on pure and Mn-doped $BaTiO_3$ nanofibers, by means of piezoresponse force microscopy in an atomic force microscope, confirming the polar domain switching behavior of the fibers. The obtained piezoelectric coefficient d_{33} were 31 and 22 pm/V for $BaTiO_3$ and $BaTi_{0.90}Mn_{0.10}O_3$. Magnetic properties of the samples were probed in a superconducting quantum interference device; diamagnetic and paramagnetic behaviors were found in pure and Mn-doped samples, respectively.

*Corresponding author. Tel.: +52-614-4391128
E-mail address: francisco.espinosa@cimav.edu.mx

1. Introduction

Ferroelectric materials having the perovskite chemical formula ABO_3 have been of central importance, as they are widely recognized to belong a class of functional materials, because of an ever growing number of technological applications, such as the possibility of having multiferroic materials, i.e. ferroelectric + ferromagnetic[1-4]. Among these ferroelectric materials, barium titanate $BaTiO_3$ has been the subject of an intense worldwide research. Barium titanate is one of the best-known materials that show ferroelectric behavior at room temperature and undergoes a cubic-to-tetragonal structural phase transition at the Curie temperature T_C = 120 °C. Furthermore, modification of pure $BaTiO_3$ by defects in the crystal structure, by doping with other elements or creating vacancy sites, i.e. oxygen vacancies, opens the possibility of having multifunctional materials.

On the other hand, quasi one-dimensional materials such as nanofibers have been the subject of an intense research, and are being applied in nanostructured-based devices. Nowadays, the electrospinning technique has been recognized as a simple and straightforward way to synthesize nanofibers. The ever-growing number of synthesized nanofibers include pure ABO_3 type materials, such as $BaMnO_3$[5], $CdTiO_3$[6, 7], $LiNbO_3$[8], $BaTiO_3$[9-13], as well as doped ABO_3 structures, e.g. $Ba_{0.6}Sr_{0.4}TiO_3$[14], $Ba_{1-x}La_xTiO_3$[15], (Mn, Mg)-doped $BaTiO_3$[16], Fe-doped $BaTiO_3$[17], $BaTi_{1-x}Ni_xO_3$[18], just to mention a few of them. Among these, Mn-doped $BaTiO_3$ is presently a material of great interest, from the point of

view of technological application as well as fundamental physics research, as this compound is believed to be ferromagnetic[19-24], even though pure $BaTiO_3$ is non-magnetic. Thus the considerable amount of research on this material, synthesized as particles[19, 20, 22, 25] and thin films[26, 27], is hardly surprising.

In the study of ferroelectric domains, there are some standard characterization techniques, such as optical birefringence, transmission electron microscopy (TEM), chemical etching, and piezoresponse force microscopy (PFM)[28, 29]. Among these, PFM has been proved to be one of the most powerful techniques in the study of ferroelectric domains due to its high resolution and ability for dynamic switching[30-32].

In this work, we have synthesized pure and Mn-doped $BaTiO_3$ nanofibers by the electrospinning method. The structures were fully characterized by scanning electron microscopy (SEM), X-ray diffraction (XRD), high-resolution transmission electron microscopy (HRTEM), Raman spectroscopy, piezoresponse force microscopy (PFM) and magnetic measurements.

2. Experimental

The synthesis of $BaTi_{1-x}Mn_xO_3$ nanofibers with concentrations x = 0, 0.10 (BTO and BTO-Mn10% at) was accomplished by the electrospinning technique. A detailed description of the procedure can be found in the literature (see ref. 33 and references therein). In this work, for pure $BaTiO_3$ nanofibers (x = 0), the precursor solution was composed by barium acetate $Ba(C_2H_3O_2)_2$, titanium isopropoxide $Ti[OCH(CH_3)_2]_4$, and poly(vinylpyrrolidone) (PVP), dissolved in a solution of acetic acid CH_3COOH, Tri/Distillate water and ethanol C_2H_5OH with molar ratios 1:1:0.5:27:4:5. On the other hand, for Mn-doped $BaTiO_3$

nanofibers, the precursor solution was composed by barium acetate $Ba(C_2H_3O_2)_2$, titanium isopropoxide $Ti[OCH(CH_3)_2]_4$, manganese acetate $Mn(C_2H_3O_2)_2$, and poly(vinylpyrrolidone) (PVP), dissolved in acetic acid CH_3COOH, Tri/Distillate water and ethanol C_2H_5OH with molar ratios 1:0.9:0.1:0.5:27:4:5.

The solution was kept at room temperature and stirring for almost 2 h, and then delivered into a metallic needle. Next, the solution was ejected through a syringe by means of an infusion pump at a constant flow rate of 0.3 mL/h. The metallic needle is then connected to a high-voltage power supply and a grounded aluminum foil was placed 15 cm from the needle tip. With an applied high-voltage of 15 kV, the precursor solution jet was accelerated toward the aluminum foil, leading to the formation of $Ba(C_2H_3O_2)_2/Ti[OCH(CH_3)_2]_4$/PVP and $Ba(C_2H_3O_2)_2/Ti[OCH(CH_3)_2]_4/Mn(C_2H_3O_2)_2$/PVP composites.

The thermal stability of as-spun composite fibers was analyzed by thermogravimetric-differential scanning calorimetry (TG-DSC), using a TA Instruments Q600 thermal analyzer, operating at a heating rate of 10 °C/min.

XRD measurements were performed in a PANalytical diffractometer, choosing the Cu K-α_1 radiation (1.540598 Å). SEM images were acquired with a JEOL JSM-7401F field emission electron microscope and HRTEM images were acquired by using a JEOL JEM-2200FS field emission microscope. Further material identification was conducted by acquiring Raman spectra with a LabRam Horiba HR system. The wavelength used was the 632.8 nm from a He-Ne laser. Piezoelectric hysteresis loops were investigated by PFM, in a commercial atomic force microscope (AFM) Infinity 3D Asylum Research with an internal lock-in amplifier. The PFM was operated in vertical mode with an AC voltage at a drive frequency of 300 kHz, far below the resonance of the cantilever, applied between the

bottom electrode and the Pt/Ir conductive tip. In order to obtain the local polarization (hysteresis loops), 10 V peak-to-peak voltage was applied in Dual AC Resonance Tracking (DART) mode. Samples were deposited on a Pt-coated silicon substrate. Finally, temperature dependence of the magnetization (zero-field cooling (ZFC) and field cooling (FC) curves measured under a constant magnetic field of 20 mT) and magnetic field dependence on the magnetization *M-H* curves were obtained in a superconducting quantum interference device (SQUID) from Quantum Design.

3. Calculation Details

The phonon modes for pure $BaTiO_3$ in the tetragonal phase were calculated by ab initio methods, within the density functional theory (DFT) formalism. To this end, we used the Vienna ab initio simulation package (VASP)[34, 35], within the projector-augmented-wave (PAW) scheme[35, 36]. The set of plane waves used extended up to a kinetic energy cutoff of 550 eV. The exchange-correlation energy was taken in the generalized-gradient approximation (GGA) with the Perdew-Burke-Ernzerhof (PBE) potential[37].

Lattice-dynamic calculations of the phonon modes were performed at the Γ point of the Brillouin zone (BZ) and the direct method was used to extract the dynamical matrix, as implemented in the PHONON code[38]. These calculations provide information about the symmetry of the modes and their polarization vectors, allowing to identify the irreducible representations and the character of the phonon modes.

The ferroelectric phase of tetragonal $BaTiO_3$, at room temperature, belongs to the space group *P*4*mm* with 5 atoms in the unit cell. For the calculation of the phonon modes, we constructed a supercell of dimensions $2 \times 2 \times 3$ with 60 non-equivalent atoms, and the

structure was fully relaxed to its equilibrium configuration until the Hellmann-Feynman forces were smaller than 0.001 eV/Å. Next, the Hellmann-Feynman forces were calculated for displaced atoms. The summation over the Brillouin zone was limited to a 6 × 6 × 6 *k*-points mesh, with 18 *k*-points in the irreducible part of the Brillouin zone (IBZ).

4. Results and Discussion

Figs. 1(a)-1(b) show SEM micrographs of as-spun composite fibers, for pure and Mn-doped $BaTiO_3$, respectively. Cylindrical and randomly oriented fibers were obtained with varying diameters from tens to hundreds of nm.

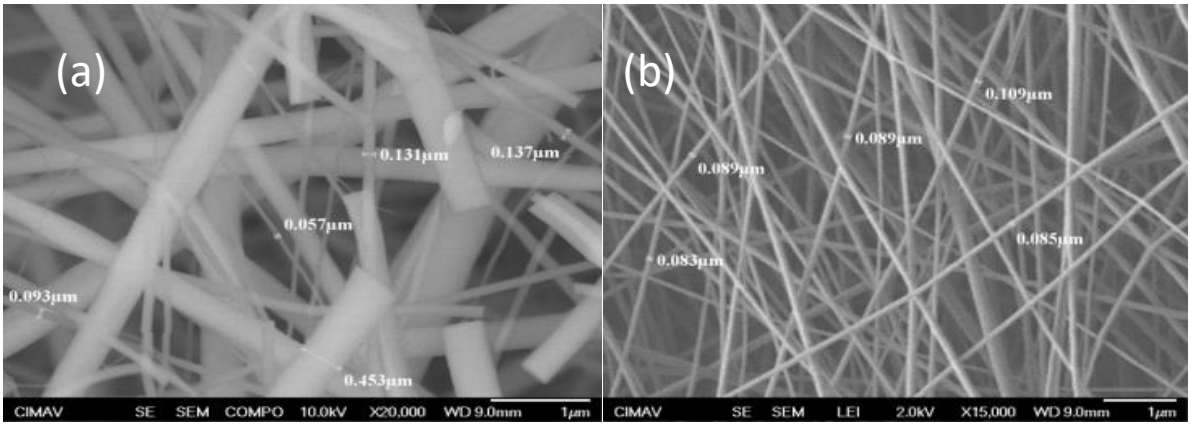

Fig. 1. SEM image of as-spun (a) $Ba(C_2H_3O_2)_2/Ti[OCH(CH_3)_2]_4/PVP$ ($x = 0$) and (b) $Ba(C_2H_3O_2)_2/Ti[OCH(CH_3)_2]_4/Mn(C_2H_3O_2)_2/PVP$ ($x = 0.10$)

Once composite nanofibers have been obtained, we choose the most suitable range of annealing temperature for the as-spun fibers, determining their thermal stability by means of TGA-DSC. On this basis, we chose 850 °C as a suitable temperature. XRD results for pure and Mn-doped $BaTiO_3$ are shown in Fig. 2. Diffraction-peak identification of $BaTiO_3$

nanofibers was performed on the basis of the PDF2 release 2010 ICDD database, card number 00-005-0626. The diffraction pattern for $BaTiO_3$ nanofibers shows that we reached the desired structure, whereas for Mn-doped $BaTiO_3$, the diffraction pattern shows additional peaks around 2θ = 26°, 37°, 41° and 49°, which can be associated with the hexagonal structure of barium titanate (h-$BaTiO_3$), according to PDF2 release 2010 ICDD database, card number 00-034-0129, in agreement with other authors[17, 19-21, 39-41]. Additionally, we observe a small peak shift to lower angles, as can be seen in the inset of Fig. 2, for the most intense peak at 2θ = 31.3°. This shift is consistent with previous studies[19], indicating that Ti^{4+} ions are substituted by Mn^{3+} ions, with ionic radii 0.605 and 0.645 Å, respectively, producing a 0.4% increase in lattice parameter.

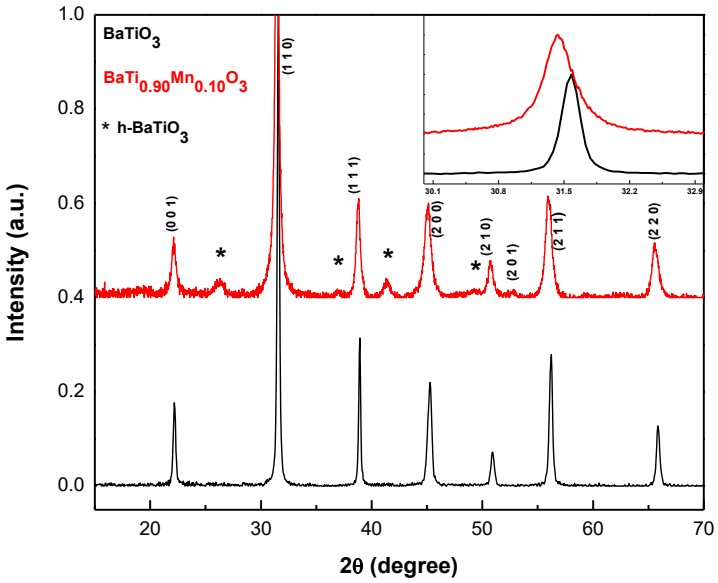

Fig. 2. Diffraction patterns of $BaTiO_3$ and $BaTi_{0.90}Mn_{0.10}O_3$. Peaks with an asterisk (*) are associated with the hexagonal phase of $BaTiO_3$. The inset shows details of the most intense peak.

Figs. 3(a)-3(b) show TEM micrographs from isolated annealed $BaTi_{1-x}Mn_xO_3$ nanofibers, for x = 0 and 0.10, respectively. Necklace-like nanofibers with diameters of varying values and typical lengths of largest fibers of the order of 3.0 and 0.9 μm for x = 0 and 0.10, were obtained. Furthermore, we found useful to probe how Mn atoms are incorporated into the structure and so we acquired an EDS mapping on doped structure. Figs. 4(a)-4(b) are the micrograph and EDS mapping from a typical nanofiber, showing Mn atoms distribution, where it can be seen that doping Mn atoms are uniformly distributed in the structure.

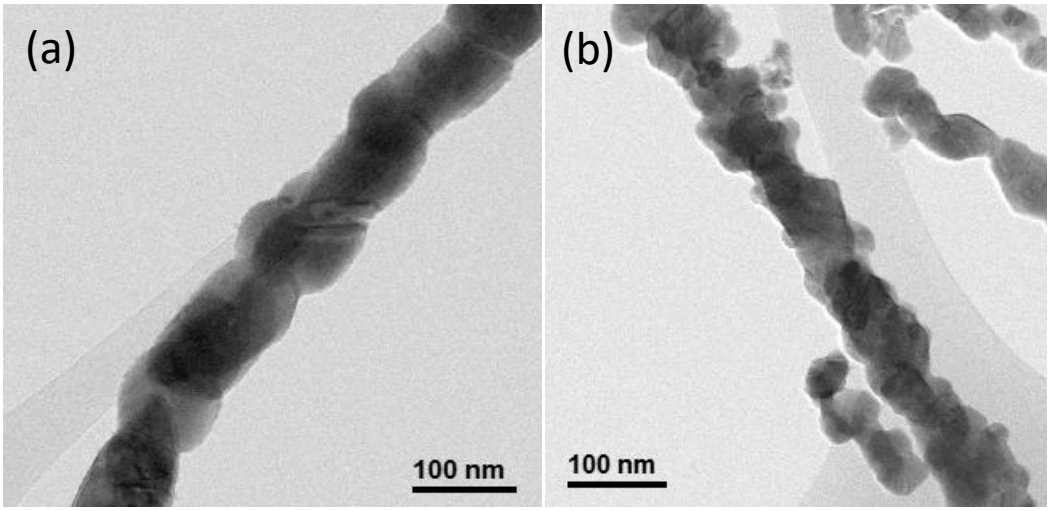

Fig. 3. TEM image of (a) pure $BaTiO_3$ nanofibers (x = 0) and (b) $BaTi_{0.90}Mn_{0.10}O_3$ nanofibers (x = 0.10)

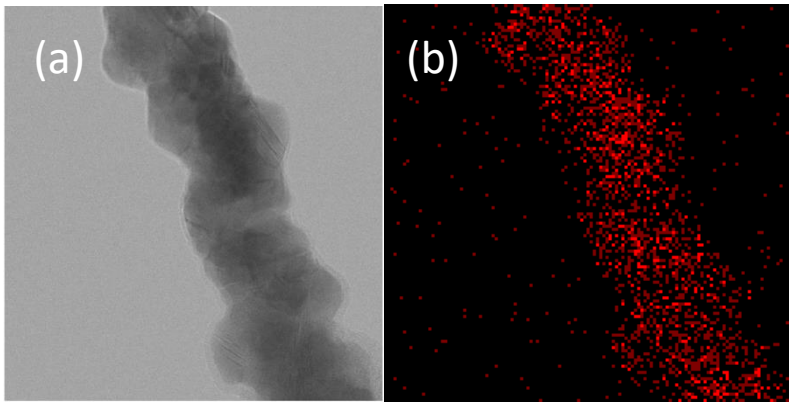

Fig. 4. Images from (a) a typical nanofibers and (b) EDS profiles showing Mn atoms distribution in doped structure.

Fig. 5 shows Raman spectra of pure and Mn-doped $BaTiO_3$ nanofibers, in the spectral range 200–800 cm^{-1}, acquired in backscattering geometry. Table 1 shows a summary of the measured Raman peaks, as well as the calculated vibrational modes for the pure structure, with their respective irreducible representations, where it can be seen a very good agreement between experimental and calculated values. Most of the irreducible representations assigned in this work coincide well with other authors[19, 20, 22, 42-46], except for the vibrating mode measured at 257 cm^{-1}, and calculated at 273 cm^{-1}, that can be assigned to mode B_1, while others authors identify it as an A_1 mode. This peak is still present in doped structure, although it has been widened and appears at ~266 cm^{-1}. The peak found experimentally in pure $BaTiO_3$ at 301 cm^{-1}, and calculated at 291 cm^{-1}, that we identify as an E(TO) mode, has been associated with the tetragonal phase[47]. In doped structure it is found at 302 cm^{-1}, indicating that even at 10 at% Mn concentrations, there is a tetragonal phase still present in the structure. Moreover, in Mn-doped structure, there appears a new peak, not found in pure $BaTiO_3$, at 629 cm^{-1}. This peak has been associated with a hexagonal phase (h-$BaTiO_3$) by some authors[19-21, 25, 40].

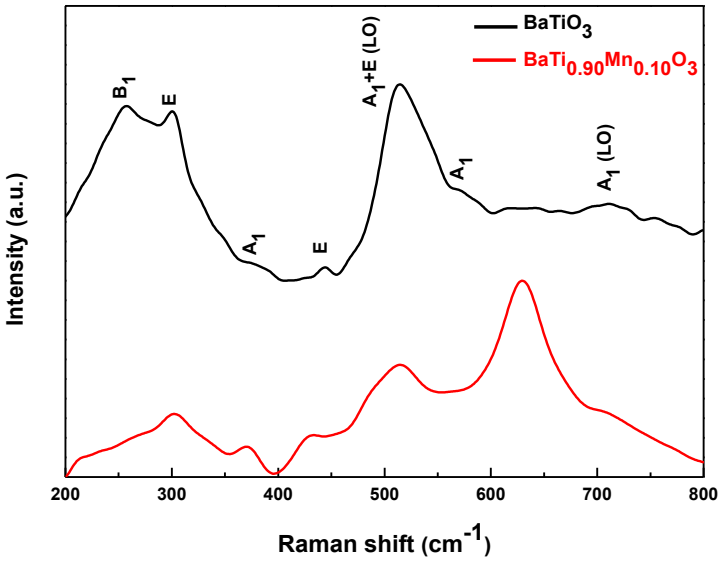

Fig. 5. Raman spectra of pure and Mn-doped $BaTiO_3$ nanofibers. Irreducible representations obtained from ab initio calculations are also shown.

Table 1. Measured frequencies (cm^{-1}) of $BaTi_{1-x}Mn_xO_3$ nanofibers for x = 0 and 0.10, and comparison with the mode frequencies calculated at the Γ point for $BaTiO_3$, together with the corresponding irreducible representations (IR)

Calculated	IR	***x***=0	***x***=0.10
273	B_1(TO)	257	266
291	E(TO)	301	302
380	A_1(TO)	375	370
450	E(TO)	444	433
512	A_1(LO)+E(LO)	515	515
557	A_1	570	-
-	-	-	629

725	A_1(LO)	711	710

Figs. 6(a)-6(b) show the AFM surface topography images for (a) $x = 0$ and (b) $x = 0.10$. The AFM images show the same morphology, i.e. necklace-like nanofibers, as already shown in HRTEM micrographs.

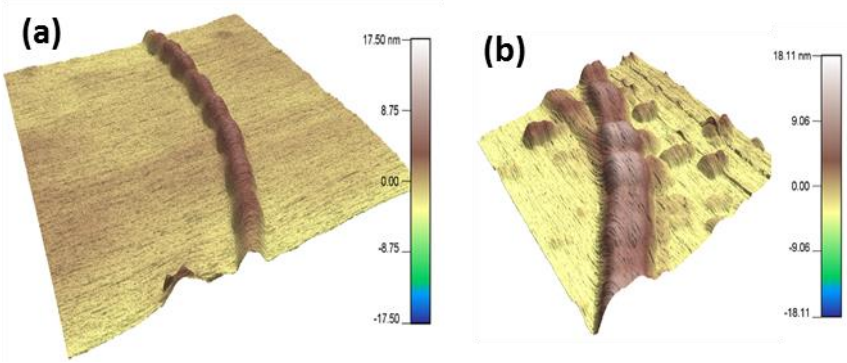

Fig. 6. AFM surface topography images of (a) $BaTiO_3$ and (b) $BaTi_{0.90}Mn_{0.10}O_3$

However, the main purpose of this AFM study is to get the piezoelectric hysteresis loops and piezoelectric constant $d_{33,}$ from where we can have evidence of the ferroelectric properties of the samples. Therefore, we used the PFM technique, which allows to locally generate piezoelectric hysteresis loops in ferroelectric materials. As is well known, with this technique the sample under study can be considered ferroelectric when its polarity can be switched by voltage bias reversals. PFM gives us characteristic phase-voltage and amplitude-voltage loops, resembling hysteresis and strain butterfly loops[48]. The variation in amplitude comes from the change of strain produced by the external field, while the alignment of dipoles in the ferroelectric crystallites are responsible for the intensity and shape of the amplitude vs. voltage loops. From the corresponding D–V butterfly curves, the d_{33}-voltage (d_{33}-V) loops can be determined through the following equation:

$$(V - V_1)d_{33} = D - D_1 \quad (1)$$

where D is the measured value of piezoelectric deformation or amplitude, V is the applied voltage, and D_1 and V_1 are the piezoelectric deformation and applied voltage of the intersection[49].

Fig. 7(a) shows the hysteresis loops of the phase versus bias applied to the samples. It is evident that the PFM phase saturates at higher voltages, confirming the characteristic ferroelectric response of the fibers. In these figures, it can be seen the difference in the ferroelectric response, being the sample with $x = 0$ more effective than sample with $x = 0.10$. This behavior is more clearly observed in the hysteresis loops of the amplitude vs. voltage in a single point, as shown in figure 7(b). The pure $BaTiO_3$ sample shows more displacement (deportation) than doped sample. The hysteresis loops of the phase vs. bias applied are very important, given that a key parameter evaluating piezoelectric performance, the d_{33} coefficient, can be obtained from these curves. Fig. 7(c) shows the values of local d_{33} coefficients (effective piezoelectric coefficients) curves as a function of AC bias voltage, for $BaTiO_3$ and $BaTi_{0.90}Mn_{0.10}O_3$ samples, in a local zone or single crystal, calculated from Eqn. (1).

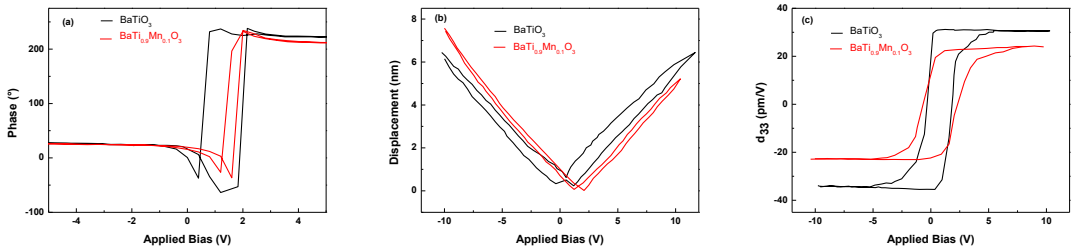

Fig. 7. Piezoresponse hysteresis loop of $BaTiO_3$ and $BaTi_{0.90}Mn_{0.10}O_3$. (a) phase, (b) amplitude and (c) d_{33} versus applied bias

Table 2 shows the results of the piezoelectric coefficients and coercive voltages for the two samples. The piezoelectric values are in very good agreement with those reported by other authors[50, 51]. The Mn-doping decreases the piezoelectric response but can, otherwise, contribute to generating a net magnetic dipole moment, as stressed by other authors[19-22], giving rise to the possibility of having a multiferroic material.

Table 2. Piezoelectric constant (d_{33}) and Coercive voltage (V_c) for pur and Mn-doped nanofibers

Sample	d_{33} [pm/V]	V_c [V]
$BaTiO_3$	31	1.89
$BaTi_{0.90}Mn_{0.10}O_3$	22	2.40

Figure 8(a) shows the *M-H* loops of the pure and Mn-doped nanofibers, exhibiting clear diamagnetic and paramagnetic behaviors, respectively. The pure paramagnetic component of the Mn-doped sample, has been obtained by subtracting the diamagnetic contribution measured from the undoped sample. Surprisingly, despite of the high Mn concentration of 10 at%, no ferromagnetism is observed in the sample. The behavior corresponds to a pure paramagnetic system. Figure 8(b) shows the zero-field cooled (ZFC) and field-cooled (FC) curves measured in a range of temperature from 5 to 350 K under an applied magnetic field of 200 Oe. The overlapping of both curves, with an average difference of 1.27×10^{-7} emu measured from the raw data, indicates that no FM order takes place in the sample[53, 54], even at low temperatures. The inset in Fig. 8(b) shows the inverse susceptibility ($1/\chi$) dependence on the temperature: $\chi = C(x)/(T - \theta_p(x))$. Where C is the Curie constant, T is

the absolute temperature, and θ_p is the paramagnetic Curie temperature. The linear fit of the data, intersects the temperature axis at -5 K indicating a Curie-Weiss paramagnetic order and the signature of a weak antiferromagnetic exchange interaction between Mn spins. It is believed that the tetragonal Mn-doped $BaTiO_3$ phase is mainly responsible for the room temperature ferromagnetism[20] by a double-exchange interaction between Mn^{3+} and Mn^{4+} ions. The appearance of a hexagonal phase decreases the ferromagnetic interactions, generated by an antiferromagnetic Mn^{3+}-Mn^{3+} pairs.

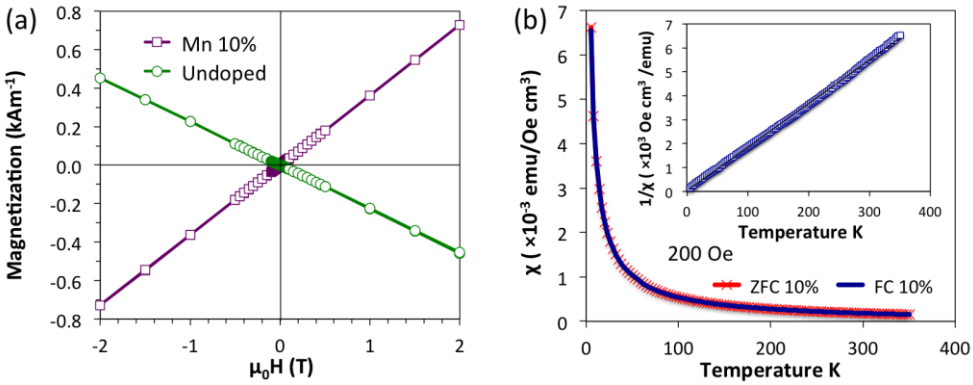

Fig. 8. (tic and paramagnetic behavior. (b) Overlapping ZFC-FC curves measured at 20 mT. The inset in (b) is the plot of the $1/\chi$ indicating a Curie-Weiss behavior with a Curie paramagnetic temperature of -5 K.

In order to calculate the magnetic moment per Mn ion and considering a high-spin state, the Curie constant has been evaluated. The S quantum number is 5/2, 2 and 3/2 for the valence states of Mn^{2+}, Mn^{3+} and Mn^{4+}, respectively.[1] Agreeing with the fact that the Mn ions doping the tetragonal phase acquire the Mn^{3+} valence state, thus the selected value for the *S* quantum number is 2. The Curie constant depends on the ion concentration and can be expressed as follows:[2]

$$C(x) = xC_0 = xN(g\mu_B)^2 S(S+1)/3k_B \quad (2)$$

where g is the Landé g-factor, x is the atomic Mn concentration equal to 0.1, N is the number of ions per unit volume, μ_B the Bohr magneton, and k_B is the Boltzmann constant. The Curie constant in our system (the inverse of the value of the slope of the straight line in the inset of Fig. 8(b)) is C = 0.0182 emu K/Oe cm^3. A recent report of bulk $BaTiO_3$ ceramics with a Mn concentration of 0.3% leads to C = 0.004858 emu K/Oe cm^3.[1] Additional values obtained in diluted systems with paramagnetic behavior are C = 0.04021 emu K/Oe cm^3 in $Zn_{0.95}Mn_{0.5}O$ and C = 0.0201 emu K/Oe cm^3 in $Zn_{0.95}Co_{0.5}O$ [Ref. 3] for sol-gel prepared bulk samples; C = 0.01633 emu K/Oe cm^3 in In_2SnO_5:Mn at a 5 at.% thin films [Ref. 4], and C = 0.0316 emu K/Oe cm^3 in $Co_{0.5}(Mg_{0.55}Zn_{0.45})_{0.5}O_{1-v}$ epitaxial thin films.[5] From the obtained Curie constant in our system and using Eq. (2) we have found a magnetic moment of 4.52μ_B/Mn ion, which is very close to the theoretical value of 4μ_B for a Mn^{3+} ion obeying the Hund's rule. The θ_p for diluted systems depends on the magnetic dopant and is described by the equation:[6]

$$\theta_p = x\theta_0 = 2xS(S+1)zJ_1/3k_B \quad (3)$$

Where Z is the coordination number, 6 in the case of Ti atoms in the tetragonal $BaTiO_3$ structure, and J_1 is the effective exchange integral between nearest Mn^{3+} ions. From the θ_p= -5 K, the J_1/k_B value is -2.08 K. This value (absolute) is smaller than that measured on $Zn_{0.95}Mn_{0.05}O$ and $Zn_{0.95}Co_{0.05}O$ of -27 and -15 K, respectively.[6]

5. Conclusions

$BaTi_{1-x}Mn_xO_3$ (x = 0, 0.10) nanofibers were synthesized by the electrospinning technique. XRD confirms the presence of a hexagonal phase for the doped structure. The presence of the vibrational mode E at 301 and 302 cm^{-1} for x = 0 and 0.10, respectively, shows that the tetragonal phase is still present, even for this high value of x. On the other hand, the PFM piezoresponse of the composite fibers showed characteristic polarization-voltage and amplitude-voltage hysteresis loops, confirming their piezoelectric hysteresis and ferroelectric switching behaviors, with piezoelectric coefficient d_{33} about 31 and 22 pm/V for pure and Mn-doped structures, respectively. Surprisingly enough, the magnetic measurements showed a paramagnetic behaviour in the doped sample, which we associate with the presence of an antiferromagnetic Mn^{3+}-Mn^{3+} coupling. The magnetic moment of 4.52μ_B/Mn ion has been calculated from the Curie constant.

Acknowledgments: The technical support of Rodrigo Domínguez, Carlos Ornelas, Wilber Antúnez, Ernesto Guerrero and Daniel Lardizábal is greatly appreciated. Ricardo López Antón and Juan A. González thank the financial support received from the Spanish MINECO (project MAT2014-58034-R).

References

1. Y. X. Wang, First-principles study on the structure instability and electronic structure of cubic $Ba_{0.5}Sr_{0.5}TiO_3$, Solid State Commun. 135 (2005) 290-293.
2. S. Rajan, P.M. Mohammed Gazzali, and G. Chandrasekaran, Impact of Fe on structural modification and room temperature magnetic ordering in BaTiO3, Spectrochimica Acta Part A: Molecular and Biomolecular Spectroscopy 171 (2017) 80-89.

3. S.G. Bahoosh, and J. M. Wesselinowa, The origin of magnetism in perovskite ferroelectric ABO_3 nanoparticles (A= K, Li; B= Ta, Nb or A= Ba, Sr, Pb; B= Ti), Journal of Applied Physics 112 (2012) 053907.

4. C.A. Díaz-Moreno, R. Farías-Mancilla, J. A. Matutes-Aquino, J. Elizalde-Galindo, F. Espinosa-Magaña, J. González-Hernández, and A. Hurtado-Macías, Magnetic behavior in $LiNbO_3$ nanocrystallites caused by oxygen vacancies, Journal of Magnetism and Magnetic Materials 356 (2014) 82-86.

5. K. Hayat, M.A. Rafiq, M.M. Hasan, Synthesis and optimization of barium manganate nanofibers by electrospinning, Ceramics International 38 (2012) 1441-1445.

6. M. S. Hassana, T. Amnab, M. Khil, Synthesis of High aspect ratio $CdTiO_3$ nanofibers via electrospinning: characterization and photocatalytic activity, Ceramics International 40 (2014) 423-427.

7. Z. Imran, S.S. Batool, M.Q. Israr, J.R. Sadaf, M. Usman, H. Jamil, M.Y. Javed, M.A. Rafiq, M.M. Hasan, O. Nur, M. Willander, Fabrication of cadmium titanate nanofibers via electrospinning technique, Ceramics International 38 (2012) 3361-3365.

8. M.C. Maldonado-Orozco, M.T. Ochoa-Lara, J.E. Sosa-Márquez, S.F. Olive-Méndez, F. Espinosa-Magaña, Synthesis and characterization of electrospun $LiNbO_3$ nanofibers, Ceramics International 41 (2015) 14886-14889.

9. J.T. McCann, J.I.L. Chen, D. Li, Z. Ye, Y. Xia, Electrospinning of polycrystalline barium titanate nanofibers with controllable morphology and alignment, Chemical Physics Letters 424 (2006) 162-166.

10. P. Sá, J. Barbosa, I. Bdikin, B. Almeida, A.G. Rolo, E. Gomes, M. Belsley, A.L. Kholkin and D. Isakov, Ferroelectric characterization of aligned barium titanate nanofibers, J. Phys. D: Appl. Phys. 46 (2013) 105304.

11. B. Sahoo, P.K. Panda, Preparation and characterization of barium titanate nanofibers by electrospinning, Ceramics International 38 (2012) 5189-5193.

12. J. Yuh, J.C. Nino, W.M. Sigmund, Synthesis of barium titanate ($BaTiO_3$) nanofibers via electrospinning, Materials Letters 59 (2005) 3645-3647.

13. Y. Wei, Y. Song, X. Deng, B. Han, X. Zhang, Y. Shen, Yuanhua Lin, Dielectric and Ferroelectric Properties of $BaTiO_3$ Nanofibers Prepared via Electrospinning, Journal of Materials Science & Technology 30 (2014) 743-747.

14. S. Maensiri, W. Nuansing, J. Klinkaewnarong, P. Laokul, J. Khemprasit, Nanofibers of barium strontium titanate (BST) by sol–gel processing and electrospinning, Journal of Colloid and Interface Science 297 (2006) 578-583.
15. P. S. Dobal, A. Dixit and R. S. Katiyar, Effect of lanthanum substitution on the Raman spectra of barium titanate thin films, J. Raman Spectrosc. 38 (2007) 142–146.
16. J. Jeong, Y.H. Han, Electrical Properties of Acceptor Doped $BaTiO_3$, Journal of Electroceramics 13 (2004), 549–553.
17. D.P. Dutta, M. Roy, N. Maitib and A.K. Tyagi, Phase evolution in sonochemically synthesized Fe^{3+} doped $BaTiO_3$ nanocrystallites: structural, magnetic and ferroelectric characterization, Phys. Chem. Chem. Phys. 18 (2016) 9758-9769.
18. S. K. Das, R.N. Mishra, B.K. Roul, Magnetic and ferroelectric properties of Ni doped $BaTiO_3$, Solid State Communications 191 (2014) 19-24.
19. N. V. Dang, T. Phan, T. D. Thanh, V. D. Lam, and L. V. Hong, Structural phase separation and optical and magnetic properties of $BaTi_{1-x}Mn_xO_3$ multiferroics, Journal of Applied Physics 111 (2012) 113913.
20. T. Phan, P. Zhang, D. Grinting, S. C. Yu, N. X. Nghia, N. V. Dang, and V. D. Lam, Influences of annealing temperature on structural characterization and magnetic properties of Mn-doped $BaTiO_3$ ceramics, Journal of Applied Physics 112 (2012) 013909.
21. A. Rani, J. Kolte, P. Gopalan, Phase formation, microstructure, electrical and magnetic properties of Mn substituted barium titanate, Ceramics International 41 (2015) 14057-14063.
22. X. Tong, Y. Lin, S. Zhang, Y. Wang, and C. Nan, Preparation of Mn-doped BaTiO3 nanoparticles and their magnetic properties, Journal of Applied Physics 104 (2008) 066108.
23. Y. Shuai, S. Zhou, D. Bürger, H. Reuther, I. Skorupa, V. John, M. Helm, H. Schmidt, Decisive role of oxygen vacancy in ferroelectric versus ferromagnetic Mn-doped $BaTiO_3$ thin films, Journal of Applied Physics 109 (2011) 084105.
24. Y.H. Lin, J. Yuan, S. Zhang, Y. Zhang, J. Liu, Y. Wang, C.W. Nan, Multiferroic behavior observed in highly orientated Mn-doped $BaTiO_3$ thin films, Applied Physics Letters 95 (2009) 3105.

25. X. Zhao, W. Chen, L. Zhang, J. Gao, L. Zhong, Effect of fabrication routes on the microstructure, the dielectric and ferroelectric properties of the Mn-doped $BaTiO_3$ ceramics, Appl. Phys. A 118 (2015) 931-938.
26. D. Bin-Feng and Z. Sheng-Qiang, The coexistence of ferroelectricity and ferromagnetism in Mn-doped $BaTiO_3$ thin films, Chin. Phys. B 20 (2011) 127701.
27. J. P. Chu, T. Mahalingam, C. F. Liu, S. F. Wang, Preparation and characterization of Mn-doped $BaTiO_3$ thin films by magnetron sputtering, J. Mater. Sci. 42 (2007) 346-351.
28. A. Gruverman, O. Auciello, R. Ramesh, H. Tokumoto, Scanning Force Microscopy of Domain Structure in Ferroelectric Thin Films: Imaging and Control, Nanotechnology 8 (1997) A38.
29. C.S. Ganpule, V. Nagarajan, H. Li, A.S. Ogale, D.E. Steinhauer, S. Aggarwal, R. Ramesh, P.D. Wolf, Role of 90° Domains in Lead Zirconate Titanate Thin Films, Appl. Phys. Lett. 77 (2000), 292.
30. A. Gruverman, O. Auciello, H. Tokumoto, Imaging and Control of Domain Structures in Ferroelectric Thin Films Via Scanning Force Microscopy, Annu. Rev. Mater. Sci. 28 (1998) 101−124.
31. T. Jungk, A. Hoffmann, E. Soergel, Quantitative Analysis of Ferroelectric Domain Imaging with Piezoresponse Force Microscopy, Appl. Phys. Lett. 89 (2006) 1−3.
32. E. Soergel, Piezoresponse force microscopy, J. Phys. D: Appl. Phys. 44 (2011) 1−17.
33. S. Thenmozhi, N. Dharmaraj, K. Kadirvelu, Hak Yong Kim, Electrospun nanofibers: New generation materials for advanced applications, Materials Science and Engineering:B 217 (2017) 36-48.
34. G. Kresse, J. Furthmuller, Efficient iterative schemes for *ab initio* total-energy calculations using a plane-wave basis set, Phys. Rev. B 54 (1996) 11169.
35. G. Kresse, D. Joubert, From ultrasoft pseudopotentials to the projector augmented-wave method, Phys. Rev. B 59 (1999) 1758.
36. P.E. Blochl, Projector augmented-wave method, Phys. Rev. B 50 (1994) 17953.
37. J.P. Perdew, K. Burke, M. Ernzerhof, Generalized Gradient Approximation Made Simple**,** Phys. Rev. Lett. 77 (1996) 3865.
38. K. Parlinski, Computer Code PHONON. See www.computingformaterials.com/index.html

39. H. T. Langhammer, T. Müller, K.H. Felgner, and H.P. Abicht, Crystal Structure and Related Properties of Manganese-Doped Barium Titanate Ceramics, J. Am. Ceram. Soc. 83 (2000) 605-611.

40. A. Kirianov, N. Ozaki, H. Ohsato, N. Kohzu, and H. Kishi, Studies on the Solid Solution of Mn in $BaTiO_3$, Jpn. J. Appl. Phys. 40 (2001) 5619-5623.

41. Y. C. Wu, S. F. Wang, and S. H. Chen, Microstructural Investigation of $BaTi_{1-x}Mn_xO_3$ Ceramics with 6H- and 12R-Polytypes, J. Am. Ceram. Soc. 92 (2009) 2099-2108.

42. Y. Zhang, J. Hao, C.L. Mak, X. Wei, Effects of site substitutions and concentration on upconversion luminescence of Er^{3+}-doped perovskite titanate, Optics express 19 (2011) 1824-9.

43. H. Hayashi, T. Nakamura, T. Ebina, In-situ Raman spectroscopy of $BaTiO_3$ particles for tetragonal-cubic transformation, Journal of Physics and Chemistry of Solids 74 (2013) 957-62.

44. U. D. Venkateswaran, V. M. Naik, and R. Naik, High-pressure Raman studies of polycrystalline $BaTiO_3$, Phys. Rev. B 58 (1998) 14256.

45. S. Fuentes, F. Cespedes, P. Munoz, E. Chavez, L. Padilla-Campos, Synthesis and structural characterization of nanocrystalline $BaTiO_3$ at various calcination temperatures, Journal of the Chilean Chemical Society 58 (2013) 2077-81.

46. M.B. Smith, K. Page, T. Siegrist, P.L. Redmond, E.C. Walter, R. Seshadri, L.E. Brus, M.L. Steigerwald, Crystal structure and the paraelectric-to-ferroelectric phase transition of nanoscale $BaTiO_3$, Journal of the American Chemical Society 130 (2008) 6955-63.

47. C.H. Perry, D.B. Hall, Temperature Dependence of the Raman Spectrum of $BaTiO_3$, Physical Review Letters 15 (1965) 700.

48. Avinash Baji, Yiu-Wing Mai, Qian Li, Yun Liu, Nanoscale investigation of ferroelectric properties in electrospun barium titanate/polyvinylidene fluoride composite fibers using piezoresponse forcé microscopy, Composites Science and Technology 71 (2011) 1435–1440

49. Z. Chen, J. Huang, Y. Yang, Y. Wang, Y. Wu, H. He, X. Wei, Z. Ye, H. Zeng, H. Cong and Z. Jiang, RSC Adv., 2 (2012) 7380.

50. B. Negulescu, C. J. M. Daumont, J. Sakai, A. Ruyter, M. Bavencoffe, N. Alyabyeva & J. Wolfman, Nonlinear piezoelectric properties of epitaxial BaTiO3 thin film, FERROELECTRICS 514 (2017) 9–18.

51. Y. Zhuang, F. Li, G. Yang, Z. Xu, J. Li, B. Fu, Y. Yang, and S. Zhang, Fabrication and Piezoelectric Property of $BaTiO_3$ Nanofibers, J. Am. Ceram. Soc., 97 (2014) 2725–2730.

53. D. P. Norton, S. J. Pearton, A. F. Hebard, N. Theodoropoulou, L. A. Boatner, and R. G. Wilson, Ferromagnetism in Mn-implanted ZnO:Sn single crystals, Appl. Phys. Lett. 82 (2003) 239.

54. S. Zhou, K. Potzger, H. Reuther, K. Kuepper, W. Skorupa, M. Helm, and J. Fassbender, Absence of ferromagnetism in V-implanted ZnO single crystals, Journal of Applied Physics 101 (2007) 09H109.

---

1 H. Yabuta, H. Tanaka, T. Furuta, T. Watanabe, M. Kubota, T. Matsuda, T. Ifuku, and Y. Yoneda, Enhancement of tetragonal anisotropy and stabilisation of the tetragonal phase by Bi/Mn-doubledoping in $BaTiO_3$ ferroelectric ceramics, Sci. Rep. 7 (2017) 45842.

2 M. I. B. Bernardi, A. Mesquita, F. Béron, K. R. Pirota, A. O. de Zevallos, A. C. Doriguetto and H. B. de Carvalho, The role of oxygen vacancies and their location in the magnetic properties of Ce1xCuxO2d nanorods, Phys. Chem. Chem. Phys. 17 (2015) 3072.

3 A. Manivannan, P. Dutta, G. Glaspell, and M. S. Seehra, Nature of magnetism in Co- and Mn-doped ZnO prepared by sol-gel technique, J. Appl. Phys. 99 (2006) 08M110.

4 M. Venkatesan, R. D. Gunning, P. Stamenov, and J. M. D. Coey, Room temperature ferromagnetism in Mn- and Fe-doped indium tin oxide thin films, J. Appl. Phys. 103 (2008) 07D135.

5 D. Zhu, Q. Cao, R. Qiao, S. Zhu, W. Yang, W. Xia, Y. Tian, G. Liu, and S. Yan, Oxygen vacancies controlled multiple magnetic phases in epitaxial single crystal $Co_{0.5}(Mg_{0.55}Zn_{0.45})_{0.5}O_{1-v}$ thin films.

6 J. H. Kim, W. K. Choo, H. Kim, D. Kim and Y. E. Ihm, Magnetoresistance and magnetic behaviors of the oxide-diluted magnetic semiconductor $Zn_{1-x}Co_xO$ thin films. J. Korean Phys. Soc. 42 (2003) S258-S262.